



Research Paper

Polyoxometalate/TiO₂/Ag composite nanofibers with enhanced photocatalytic performance under visible light



Hongfei Shi^{a,b}, Yanchun Yu^a, Yi Zhang^a, Xiaojia Feng^{a,c,*}, Xinyu Zhao^a, Huaqiao Tan^{a,*}, Shifa Ullah Khan^a, Yangguang Li^a, Enbo Wang^{a,*}

^a Key Laboratory of Polyoxometalate Science of Ministry of Education, Faculty of Chemistry, Northeast Normal University, Changchun, 130024, PR China

^b Institute of Petrochemical Technology, Jilin Institute of Chemical Technology, Jilin, 132022, PR China

^c College of Science, Shenyang Agricultural University, Shenyang, 110866, PR China

ARTICLE INFO

Keywords:

Titanium dioxide
Polyoxometalates
Silver nanoparticle
Nanofiber
Photocatalysis

ABSTRACT

The exploration of highly efficient and stable visible-light-driven photocatalysts for the wastewater treatment has been recognized as one of the currently most challenging topics for the environment remediation. In this paper, we report a new type of polyoxometalate-TiO₂ composite nanofibers loaded with Ag nanoparticles (NPs), labeled as PMo₁₂/TiO₂/Ag-X (PMo₁₂ = [PMo₁₂O₄₀]³⁻; X represents the weight percent (%) of Ag in PMo₁₂/TiO₂/Ag samples; X = 3.98, 5.41, 6.83, and 7.19 respectively). The SEM and TEM images manifest that the average diameter of the PMo₁₂/TiO₂ composite fibers is about 130 ± 30 nm, and the average size of Ag NPs is about 15 ± 5 nm. Photocatalytic experiments confirm that PMo₁₂/TiO₂/Ag catalysts display highly efficient and durable activity for the photodegradation of methyl orange (MO) and photoreduction of Cr(VI) under visible light irradiation (λ > 420 nm). In these composite series, PMo₁₂/TiO₂/Ag-5.41 exhibits the highest photocatalytic activity. The photocatalytic mechanism reveals that both Ag and PMo₁₂ can be excited under visible light irradiation, which greatly improves the visible-light absorption of the composites. Furthermore, the introduction of POM species can not only improve the light adsorption and redox activity of the TiO₂, but also promote the photochemical stability of the plasmonic composites because of the relatively narrow band gap and low reversible redox potential of polyoxoanion. Such POMs-based plasmon photocatalysts are important in ongoing efforts to designing and exploring of new photocatalytic materials with low cost, high efficiency, and durability.

1. Introduction

The removal of pollutants from water has received considerable attention over the past few decades due to the urgent requirement of environmental improvement. Wastewater usually contains organic pollutants (such as organic dyes, pesticides, and antibiotics) and inorganic pollutants (exemplified by heavy metal ions Cr, Cd, and Pb etc.), which have caused serious environmental problems because of their toxicity, persistence and bioaccumulation [1–6]. Removing the pollutants generally include physical, chemical, and biological methods. In this research field, photocatalytic treatment is currently one of the most promising and efficient ways to decontaminate the pollutants. In such a subfamily, TiO₂ is the one of the most widely used and studied photocatalyst owing to its low cost, nontoxicity, high oxidation ability, efficient photocatalytic properties, and photochemical stability [2,3,7]. However, two inherent drawbacks of TiO₂ have

hindered its practical application in photocatalysis, that is, the relatively wide band gap (3.2 eV) and the low photo-induced charge carriers separation efficiency [8]. Therefore, considerable efforts have been paid to improve the catalytic performances of TiO₂, particularly from the morphology engineering [9–11], metal or non-metal element doping [12–15], semiconductor coupling and others [16–21].

Besides the above approaches, constructing of metal/TiO₂ (metal = Ag, Pt, Au, Pd etc.) plasmonic photocatalysts has also aroused great interests of researchers. The noble metal nanoparticles (NPs) exhibit intense surface plasmon resonance (SPR) absorption in visible region and high electron trapping ability, which can improve the photocatalytic activity of the composites under visible light irradiation [22–25]. Among them, silver has been widely used in SPR photocatalysis because of its relatively low price, excellent conductivity, wide SPR absorption and intense local electromagnetic fields caused by SPR [27,28]. In the past few years, plenty of Ag-modified TiO₂ with various

* Corresponding authors at: Key Laboratory of Polyoxometalate Science of Ministry of Education, Faculty of Chemistry, Northeast Normal University, Renmin Street No. 5268, Changchun, Jilin Province, 130024, PR China.

E-mail addresses: fengxiaojia003@126.com (X. Feng), tanhq870@nenu.edu.cn (H. Tan), wangeb889@nenu.edu.cn, wangeb889@hotmail.com (E. Wang).

<http://dx.doi.org/10.1016/j.apcatb.2017.09.027>

Received 8 May 2017; Received in revised form 6 September 2017; Accepted 11 September 2017

Available online 14 September 2017

0926-3373/ © 2017 Published by Elsevier B.V.

morphologies and good photocatalytic activities have been fabricated [29–35]. However, most of these Ag/TiO₂ composites are unstable in the photocatalytic process due to the poor response of TiO₂ in visible light region, while Ag might be oxidized by its own plasmonic holes, leading to the deactivation of catalysts. Therefore, it is still a great challenge to further improve the photocatalytic efficiency and durability of these Ag/TiO₂ SPR photocatalysts.

Polyoxometalates (POMs), a class of well-defined early transition metal-oxygen clusters with unique structural features and tunable band gap structures, have been considered as an ideal candidate to respond above problems [36,37]. Usually, POMs can undergo a stepwise multi-electron reversible redox process with negligible structural changes [38]. They also possess semiconductor-like features with regulated electronic characteristics and energy levels (its LUMO and HOMO, corresponding to the CB and VB of semiconductor) [39–45]. Thus, the combination of POMs and TiO₂ can not only modulate the light adsorption and redox activity of the composites, but also facilitate the *in situ* loading of noble metal particles and improve the photoreduction activity of TiO₂. So far, a series of POMs/TiO₂ composites have been reported, which have exhibited enhanced photocatalytic performance with respect to that of TiO₂ [46–55]. However, most of these photocatalysts are still limited to work under UV light irradiation ($\lambda < 380$ nm) due to the wide band gaps of both POMs and TiO₂ [49–52]. The explorations on the highly efficient visible-light-response POMs/TiO₂ photocatalysts are scarcely reported [53–55].

Based on the above considerations, we attempt to construct new ternary POM/TiO₂/Ag composite photocatalysts. Considering that H₃PMo₁₂O₄₀ (abbr. PMo₁₂) possesses a band gap of 2.4 eV and exhibits an obvious visible-light absorption in the range of 400–516 nm [45], we select PMo₁₂ as the precursor to combine with TiO₂. During the preparation, a facile electrospinning/calcination method was employed to fabricate PMo₁₂/TiO₂ composite nanofibers. Then, Ag NPs were further *in situ* photodeposited on the surface of PMo₁₂/TiO₂ nanofibers, forming the ternary PMo₁₂/TiO₂/Ag-X (X = 3.98, 5.41, 6.83 and 7.19 respectively) composite materials. Photocatalytic experiments reveal that the PMo₁₂/TiO₂/Ag composites exhibit highly efficient photocatalytic performance for the degradation of methyl orange and photoreduction of Cr(VI) under visible-light irradiation ($\lambda > 420$ nm), which performance is obviously higher than that of precursor TiO₂, PMo₁₂/TiO₂ and TiO₂/Ag. In addition, the PMo₁₂/TiO₂/Ag-5.41 exhibits the best photocatalytic performance among the above composites. The durability and the possible photocatalytic mechanism of such composites have also been investigated.

2. Experimental section

2.1. Chemicals and materials

All chemicals were used without any further purification. Tetrabutyltitanate (TBT), Na₂SO₄, AgNO₃, CH₃CH₂OH, H₃PMo₁₂O₄₀, C₃H₇OH, CH₃COOH, triethanolamine (C₆H₁₅NO₃), 4-hydroxy-TEMPO, K₃[Fe(CN)₆], K₂Cr₂O₇, methyl orange (MO), KCl, BaSO₄, and K₄[Fe(CN)₆] were obtained from Aladdin Chemical Co., Ltd., China. Polyvinylpyrrolidone (PVP, Mw \approx 1,300,000) was purchased from Alfa Aesar Inc.

2.2. Preparation of PMo₁₂/TiO₂ nanofiber composites

In a typical preparation step, 0.7 g of PVP was dissolved in 15 mL CH₃CH₂OH with vigorous stirring for 3 h to form a clear solution. 0.2 mL CH₃COOH and 0.4 mL TBT were added with stirring. Then calculated amount of H₃PMo₁₂O₄₀ (5–30 mol% relative to TBT) was added into the above solution, and it was stirred to form settled solution. The mixed solution was put into a 20 mL plastic syringe for electrospinning. A 15 kV electrical potential was applied with an electrode distance of 15 cm, and an aluminum foil was used as collector.

The solution was ejected at a rate of 0.5 mL h⁻¹ controlled with a syringe pump to obtain the electrospun nanofibers. The obtained nanofibers were calcined at 400–550 °C at a heating rate of 2 °C min⁻¹ for 5 h in air to remove PVP. TiO₂ nanofibers with different content of PMo₁₂ have been fabricated through this method. These samples are labeled as PMo₁₂/TiO₂ (X Y), Where X and Y values represent the molar ratio of PMo₁₂ to TBT and the calcination temperature, respectively. Based on above method, the pure TiO₂ nanofibers without the addition of PMo₁₂ were also prepared as the contrast sample.

2.3. Preparation of PMo₁₂/TiO₂/Ag composites

In a typical preparation step, 0.2 g of PMo₁₂/TiO₂ (20% 450 °C) composite nanofibers were dispersed into a 100 mL aqueous solution containing 50 mL isopropanol, followed by sonication for 20 min. The suspension was irradiated with a 300 W Xe lamp (CEL-HXF300, AULIGHT) for 1 h. The solution gradually became dark blue. Then, designed amount of AgNO₃ aqueous solution (20 mM L⁻¹) was added into the above solution with vigorous magnetic stirring for additional hour. Then, the color of solution became brown. The PMo₁₂/TiO₂/Ag composite materials were collected, washed with deionized water and ethanol, and dried at 70 °C for 12 h. According to the EDX data in Figs. 1 (f) and S1, the as-obtained samples were labeled as PMo₁₂/TiO₂/Ag-X (X stands for the weight percent (%) of Ag loaded in PMo₁₂/TiO₂/Ag samples; X = 3.98, 5.41, 6.83, and 7.19 respectively). Following the same preparation route, the TiO₂/Ag contrast sample was also prepared by using the aforementioned pure TiO₂ nanofibers.

2.4. Characterization

The morphologies of these composite photocatalysts were characterized with a JEOL JSM 4800F SEM coupled with an energy-dispersive X-ray (EDX) spectrometer. TEM (transmission electron microscopy) and HRTEM images were measured on a JEM-2100F microscope operated at 200 kV. X-ray photoelectron spectrum (XPS) analyses were performed on an ESCALABMKII spectrometer with an Al-K α (1486.6 eV) achromatic X-ray source. The UV–vis diffuse reflectance spectra (DRS) was collected on a Shimadzu UV-2600 UV–vis spectrophotometer. The BET specific surface areas were measured on a Micrometrics ASAP-2020 Automatic specific surface area and porous physical adsorption analyzer. X-Ray diffraction (XRD) patterns were recorded on a Bruker AXS D8 Focus using filtered Cu K α radiation ($\lambda = 1.54056$ Å). The photoluminescence (PL) spectra was performed at room temperature on a Hitachi F-4600 spectrophotometer with an excitation wavelength 380 nm.

2.5. Photoelectrochemical measurements

The photocurrent measurements were conducted on a CHI660E Electrochemical Workstation (Shanghai Chenhua Instrument Corp., China) with a conventional three-electrode configuration in a quartz cell. A Pt foil and Hg/Hg₂Cl₂ electrode were served as the counter electrode and reference electrode, respectively. A 300 W Xe lamp (CEL-HXF300, AULIGHT) was used as the light source. A 0.5 M Na₂SO₄ aqueous solution was applied as the electrolyte. Typically, the working electrodes were prepared as follows: 50 mg of the as-prepared photocatalysts was dispersed into 5 mL ethanol with sonication for 25 min to make a slurry. Next, 0.5 mL of the solution was uniformly dropped onto a 1 \times 4 cm² FTO glass substrate. The working electrode prepared with the sample has an active area of ca. 3 cm². Finally, the prepared electrodes were dried at 70 °C for 3 h to obtain the working electrodes.

2.6. Electrochemical impedance spectroscopy (EIS) measurements

EIS measurements was conducted using a Model CS350 electrochemistry station (Wuhan CorrTest Instrument Corporation) in 0.1 M

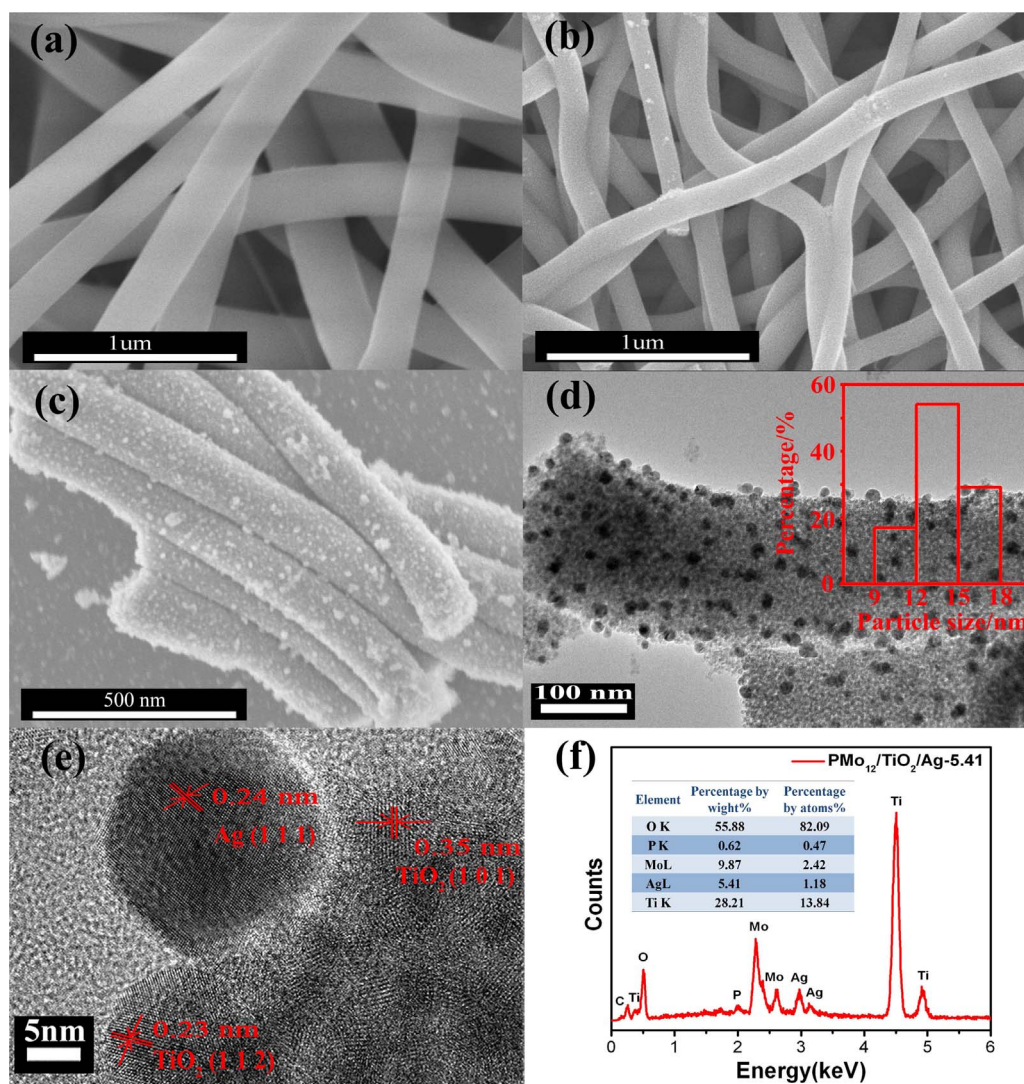


Fig. 1. SEM images of PVP/PMo₁₂/TiO₂ nanofibers (20 mol% Mo/Ti) before calcination (a) and after calcination at 450 °C (b); The photographs of SEM (c), TEM (d) and HRTEM (e) for PMo₁₂/TiO₂/Ag-5.41; (f) the EDX of PMo₁₂/TiO₂/Ag-5.41.

KCl solution containing 5 mM Fe(CN)₆^{3−/4−} with a frequency range from 0.01 Hz to 10 kHz at 0.2 V. The EIS data were recorded using a conventional three-electrode system, where samples on FTO glass with an active area of ca. 1.0 cm² were prepared as the working electrode, a Pt wire as counter electrode and Ag/AgCl as a reference electrode, respectively.

2.7. Photocatalytic degradation of MO

The photocatalytic activity of as-obtained samples was estimated through the photodegradation of MO applying a glass vessel with a water-cooling jacket as reactor and a 300 W xenon-lamp with a 420 nm cut-off filter as illuminant. The irradiation distance between the mixture solution and the lamp was about 15 cm. Typically, 20 mg of PMo₁₂/TiO₂/Ag composites was dispersed into 20 mL MO (20 ppm) aqueous solution (pH = 1). Prior to irradiation, the mixture solution was stirred in darkness for 1 h to obtain the saturated absorption of MO molecules onto the catalysts, then above solution was illuminated under visible light irradiation, every 20 min, 1 mL of the suspension was withdrawn, centrifuged subsequently, and measured at the maximum absorption wavelength of 506 nm.

2.8. Photocatalytic reduction of Cr(VI)

Typically, 20 mg of photocatalyst was added into an aqueous

solution containing 20 mL of K₂Cr₂O₇ solution (160 ppm) and 20 mL isopropanol. Similarly, the suspensions were stirred in the dark for 0.5 h to obtain absorption-desorption equilibrium between the K₂Cr₂O₇ and the catalyst surface before irradiation. Then above mixture was stirred and exposed to the visible-light irradiation. At given irradiation time intervals, about 2 mL of suspension was taken out, centrifuged, and measured at a maximum absorption wavelength of 365 nm.

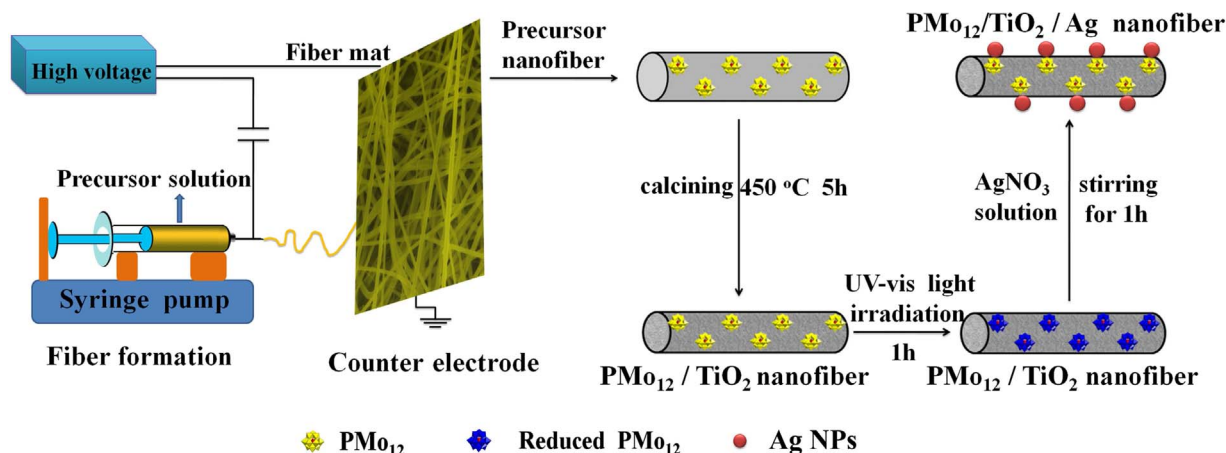
2.9. Active species trapping experiment

To detect the active species in the photocatalytic process of MO, triethanolamine (TEOA), isopropanol (IPA) and 4-hydroxy-TEMPO were employed as hole (h⁺) scavenger, hydroxyl radical (OH) scavenger and superoxide radical (O₂^{•−}) scavenger, respectively. Typically, 20 mg of photocatalyst with different scavengers was added in MO (20 mL, 20 ppm) aqueous solution, and the following processes were similar to the MO photodegradation test.

3. Results and discussion

3.1. Sample preparation

The ternary PMo₁₂/TiO₂/Ag composite nanofibers were fabricated by a facile electrospinning/calcination route, following with an *in situ* photoreduction step (as illustrated in Scheme 1). Firstly, a mixed

Scheme 1. Illustration of the synthesis of $\text{PMo}_{12}/\text{TiO}_2/\text{Ag}$ composite.

solution of PVP, $\text{H}_3\text{PMo}_{12}\text{O}_{40}$ and TBT was electrospun to form PVP- $\text{H}_3\text{PMo}_{12}\text{O}_{40}$ -TBT nanofibers. Then the nanofibers were thermally treated at 400–550 °C to remove PVP so as to form TiO_2 crystals. In this case, we investigated two important factors that can affect the formation and photocatalytic activity of the $\text{PMo}_{12}/\text{TiO}_2$ nanofibers. The one is the molar ratio of PMo_{12} to TBT, and the other is the calcination temperature. Fig. S3 shows the PXRD patterns of $\text{PMo}_{12}/\text{TiO}_2$ nanofibers with different calcination temperature and with different molar ratio of PMo_{12} to TBT. It is observed that the main characteristic diffraction peaks of all these samples are similar, which can be assigned to the crystalline anatase phase of TiO_2 (JCPDS no. 21-1272). It is noteworthy that several new diffraction peaks of the monoclinic phase MoO_3 (JCPDS no. 05-0508) are observed in the $\text{PMo}_{12}/\text{TiO}_2$ (20% 500 °C), $\text{PMo}_{12}/\text{TiO}_2$ (20% 550 °C), $\text{PMo}_{12}/\text{TiO}_2$ (25% 450 °C) and $\text{PMo}_{12}/\text{TiO}_2$ (30% 450 °C) samples, indicating that PMo_{12} was decomposed to MoO_3 at higher temperatures or with higher molar ratios of PMo_{12} to TBT. Fig. S4 displays the results of Cr(VI) photoreduction applying $\text{PMo}_{12}/\text{TiO}_2$ nanofibers as catalysts. It is obvious that the photocatalytic activity of the $\text{PMo}_{12}/\text{TiO}_2$ nanofibers has been largely improved by the introduction of PMo_{12} . Particularly, $\text{PMo}_{12}/\text{TiO}_2$ (20% 450 °C) exhibits the best photocatalytic performance. In a typical reaction system containing 40 mL of 80 ppm Cr(VI), about 96% of Cr(VI) can be reduced in 30 min by 20 mg of the photocatalyst $\text{PMo}_{12}/\text{TiO}_2$ (20% 450 °C) under the UV-vis light irradiation, which is much higher than that of pure TiO_2 nanofibers (42.16%). The photocatalytic activities of $\text{PMo}_{12}/\text{TiO}_2$ (20% 500 °C), $\text{PMo}_{12}/\text{TiO}_2$ (20% 550 °C), $\text{PMo}_{12}/\text{TiO}_2$ (25% 450 °C) and $\text{PMo}_{12}/\text{TiO}_2$ (30% 450 °C) were also lower than that of $\text{PMo}_{12}/\text{TiO}_2$ (20% 450 °C), since partial PMo_{12} was decomposed to MoO_3 during the preparation process (based on the results of XRD). According to the above results, the optimal $\text{PMo}_{12}/\text{TiO}_2$ (20% 450 °C) composite was selected as a representative in the following study. Moreover, different amount of Ag NPs was *in situ* photodeposited on the surface of the $\text{PMo}_{12}/\text{TiO}_2$ (20% 450 °C) nanofibers using different amount of AgNO_3 solution. As a result, a series of $\text{PMo}_{12}/\text{TiO}_2/\text{Ag-X}$ (X = 3.98, 5.41, 6.83, and 7.19 respectively) composite photocatalysts were prepared, and their visible-light-driven photocatalytic activities were investigated.

3.2. Composition and structure characterization

The morphology and microstructure of the PVP/ $\text{PMo}_{12}/\text{TiO}_2$ nanofibers at the optimum electrospinning conditions (20 mol% Mo/Ti) was illustrated in Fig. 1. The nanofibers before calcination exhibit a relative smooth and uniform surface. The fibers are ca. 260 ± 30 nm in diameter and several micrometers in length (Fig. 1a). After removing PVP at 450 °C, the fibrous morphology of $\text{PMo}_{12}/\text{TiO}_2$ is well maintained. As shown in Fig. 1b, these fibers become coarse and porous (Fig.

S5), and the size is reduced to 130 ± 30 nm in diameter. The corresponding elemental mapping of $\text{PMo}_{12}/\text{TiO}_2$ nanofiber is exhibited in Fig. S6, which demonstrates that the Ti, O, P, Mo elements are well-arranged over the $\text{PMo}_{12}/\text{TiO}_2$ nanofibers. The BET surface areas of pure TiO_2 and $\text{PMo}_{12}/\text{TiO}_2$ (20% 450 °C) were 162.775 and 233.163 $\text{m}^2 \text{g}^{-1}$, respectively. Such results suggest that the $\text{PMo}_{12}/\text{TiO}_2$ composite nanofibers are more beneficial for the construction of porous superstructures than pure TiO_2 nanofibers (Fig. S7). Fig. 1c and d presents the SEM and TEM images of $\text{PMo}_{12}/\text{TiO}_2/\text{Ag-5.41}$, respectively. It is found that Ag NPs have been uniformly deposited on the surface of $\text{PMo}_{12}/\text{TiO}_2$ nanofibers with the average size of 15 ± 5 nm in diameter. The high resolution TEM images of $\text{PMo}_{12}/\text{TiO}_2/\text{Ag-5.41}$ display that the crystal lattices of both TiO_2 and Ag NPs coexist in the sample (Fig. 1e). The observed lattice spacing of 0.35 nm and 0.23 nm corresponds to the (101) and (112) crystallographic planes of the anatase phase of TiO_2 (JCPDS NO. 21-1272). The interplanar distance of 0.24 nm is assigned to the lattice spacing of Ag (111) planes (JCPDS NO. 04-0783). The EDX measurements further indicate that the signals of Ti, Mo, O, P and Ag elements are all observed in the pattern of $\text{PMo}_{12}/\text{TiO}_2/\text{Ag}$ samples (Figs. 1 f and S1).

Fig. 2a presents the XRD patterns of TiO_2 , TiO_2/Ag , $\text{PMo}_{12}/\text{TiO}_2$ and $\text{PMo}_{12}/\text{TiO}_2/\text{Ag-5.41}$, respectively. The main diffraction peaks of $\text{PMo}_{12}/\text{TiO}_2/\text{Ag-5.41}$ are similar to that of $\text{PMo}_{12}/\text{TiO}_2$. The characteristic diffraction peaks at 25.3° (101), 37.8° (004), 48.1° (200), 53.9° (105), and 62.7° (204) can be assigned to the crystalline anatase phase of TiO_2 (JCPDS no. 21-1272). However, no obvious Ag NPs diffraction peaks can be assigned, which might be related to the low content of Ag or the diffraction peaks of Ag NPs are covered by the ones of TiO_2 . However, the presence of Ag NPs can be detected from the UV-vis diffuse reflectance spectra. As illustrated in Fig. 2b, TiO_2 exhibits an obvious spectra absorption onset at 400 nm, which is in accordance with the band gap of anatase TiO_2 (3.2 eV). Simultaneously, PMo_{12} shows absorption band at about 540 nm. When PMo_{12} was introduced into TiO_2 , the absorption of $\text{PMo}_{12}/\text{TiO}_2$ in the visible region has been enhanced. As Ag NPs were deposited, the visible-light absorption of $\text{PMo}_{12}/\text{TiO}_2/\text{Ag}$ composite was further improved due to the synergistic absorption of PMo_{12} and the SPR absorption of Ag NPs, which is clearly higher than that of TiO_2/Ag [26,27]. In addition, the light absorbance of $\text{PMo}_{12}/\text{TiO}_2/\text{Ag}$ in the range of 400–800 nm was gradually enhanced with the increase of Ag content. The band gap energies of as-prepared composites are estimated from the Tauc plots (Fig. S8) [56], which is 3.20, 3.14, 3.09, 3.08, 3.06, 3.03, and 3.00 eV for TiO_2 , $\text{PMo}_{12}/\text{TiO}_2$, TiO_2/Ag and $\text{PMo}_{12}/\text{TiO}_2/\text{Ag-X}$ (X = 3.98, 5.41, 6.83, 7.19) respectively. Compared with $\text{PMo}_{12}/\text{TiO}_2$, the band gaps of all Ag loaded $\text{PMo}_{12}/\text{TiO}_2$ composites were slightly decreased. It is presumed that Ag NPs may introduce the localized energy levels into the $\text{PMo}_{12}/\text{TiO}_2$ band gap, thus reducing the energy gap of $\text{PMo}_{12}/\text{TiO}_2$.

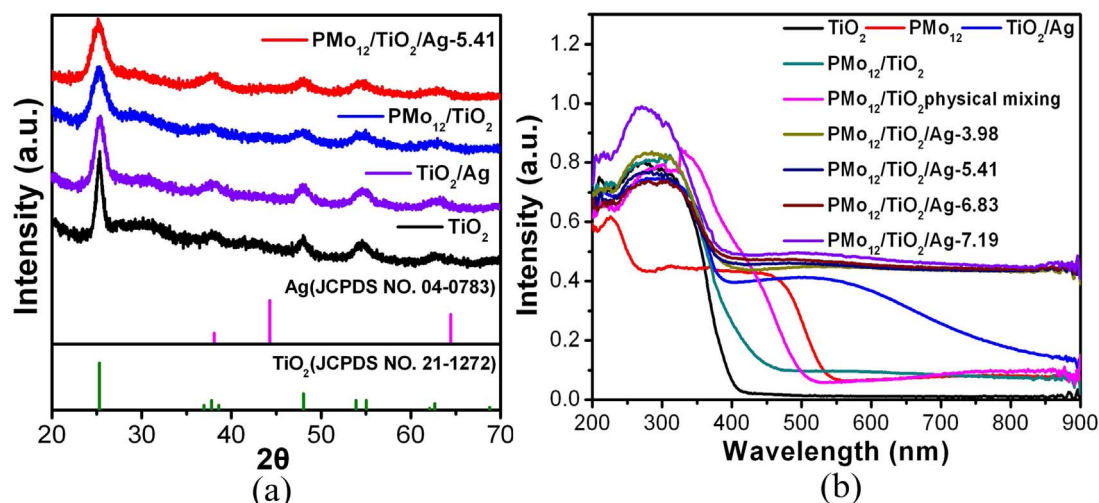


Fig. 2. (a) XRD patterns of the TiO_2 , TiO_2/Ag , $\text{PMo}_{12}/\text{TiO}_2$ and $\text{PMo}_{12}/\text{TiO}_2/\text{Ag-5.41}$; (b) The DRS of pure TiO_2 , PMo_{12} , TiO_2/Ag and $\text{PMo}_{12}/\text{TiO}_2/\text{Ag}$ samples with different Ag content.

[57,58].

XPS analysis was performed to further validate the elemental composition and the corresponding valence states in $\text{PMo}_{12}/\text{TiO}_2$ and $\text{PMo}_{12}/\text{TiO}_2/\text{Ag-5.41}$. As shown in Fig. 3a, the Ag 3d, Mo 3p, Mo 3d, Ti 2p, C 1s, P 3s and O 1s signals are apparently observed from the full

survey of $\text{PMo}_{12}/\text{TiO}_2/\text{Ag-5.41}$. In Fig. 3b, the Mo 3d_{5/2} (232.38 eV) and Mo 3d_{3/2} (235.56 eV) peaks of $\text{PMo}_{12}/\text{TiO}_2/\text{Ag-5.41}$ can be split into four peaks at 232.04 eV, 232.46 eV and 235.15 eV, 235.66 eV, respectively. The doublet peaks at 232.04 eV (Mo 3d_{5/2}) and 235.15 eV (Mo 3d_{3/2}) can be assigned to Mo (V) species, while the peaks at

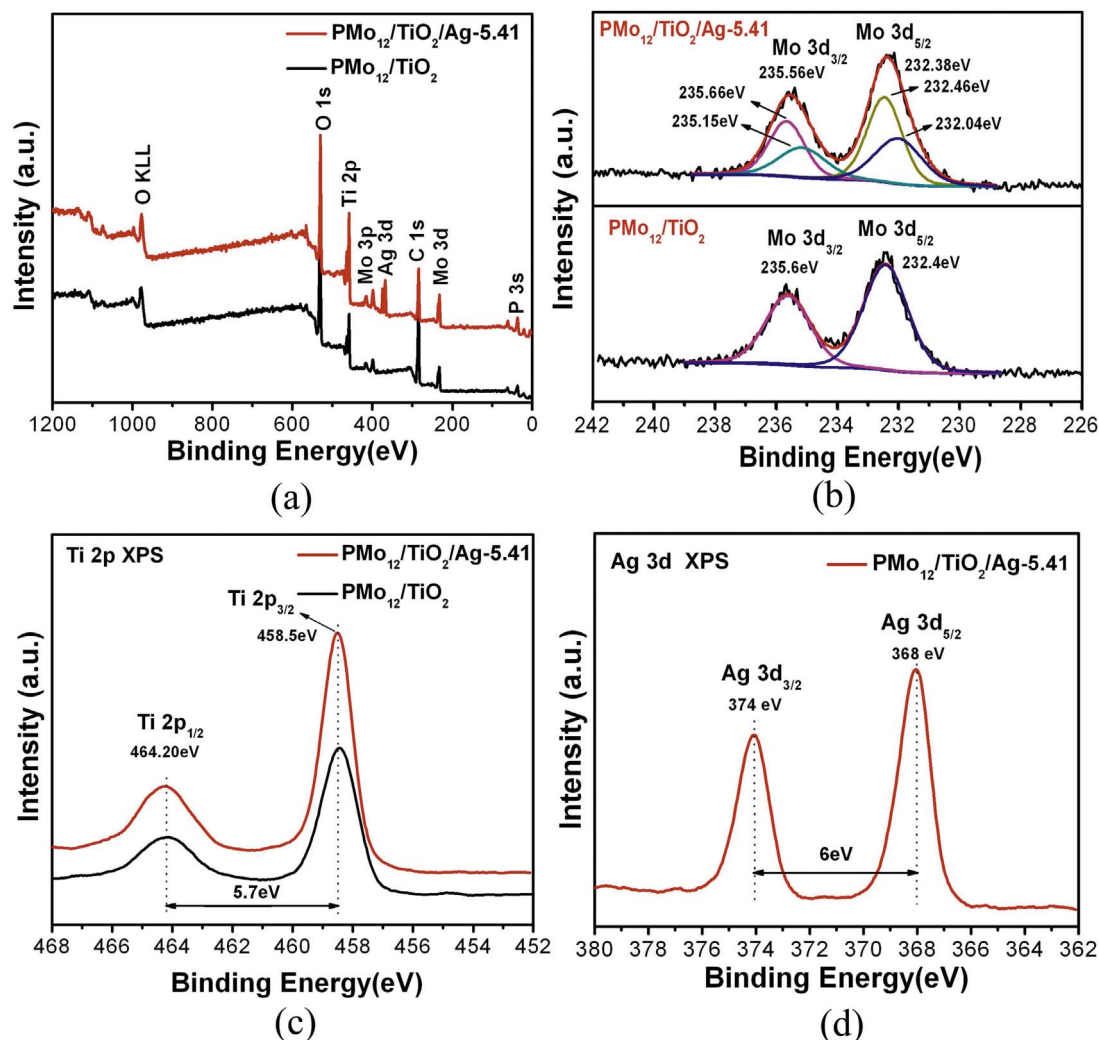


Fig. 3. XPS spectra of $\text{PMo}_{12}/\text{TiO}_2$ and $\text{PMo}_{12}/\text{TiO}_2/\text{Ag-5.41}$: (a) the full survey; (b) Mo 3d XPS; (c) Ti 2p XPS; (d) Ag 3d XPS spectrum of $\text{PMo}_{12}/\text{TiO}_2/\text{Ag-5.41}$.

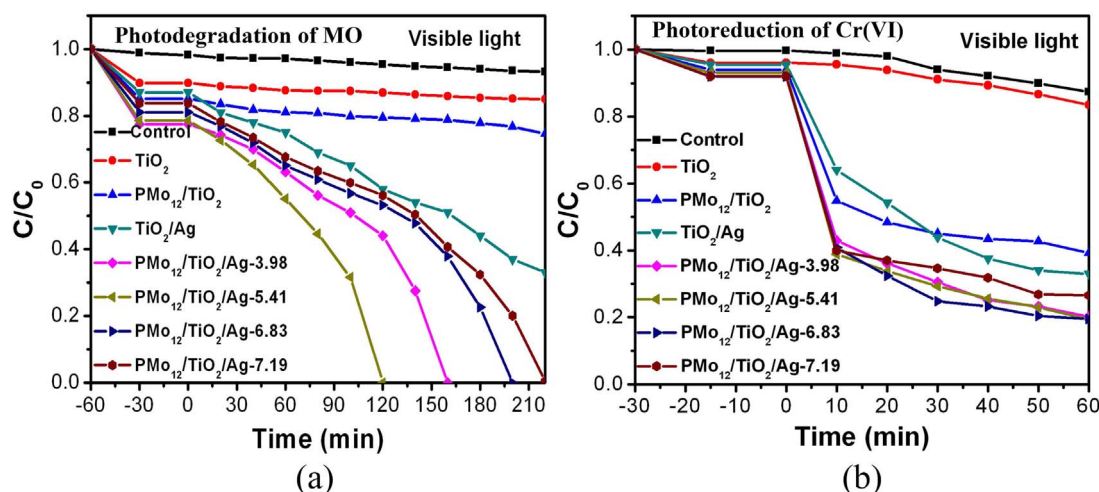


Fig. 4. The profiles of (a) photodegradation of MO and (b) photoreduction of Cr(VI) by different photocatalysts under visible-light irradiation ($\lambda > 420$ nm). C is the concentration of MO/Cr(VI) at time t , and C_0 is the concentration of MO/Cr(VI) solution before light irradiation.

232.46 eV (Mo 3d_{5/2}) and 235.66 eV (Mo 3d_{3/2}) are attributed to Mo (VI) species [59]. The existence of low valence molybdenum is due to the strong reversible redox properties of PMo₁₂, which can be easily reduced under light irradiation. In Fig. 3c, two peaks at the binding energies of 464.2 eV and 458.5 eV are assigned to Ti 2p_{1/2} and Ti 2p_{3/2}, which is consistent with the Ti (IV) [60]. Fig. 3d presents the Ag 3d XPS spectrum for the PMo₁₂/TiO₂/Ag-5.41. The peaks at the binding energies of 368.0 eV (Ag 3d_{5/2}) and 374 eV (Ag 3d_{3/2}) can be assigned to the metallic Ag (0). The 6.0 eV difference between the binding energy of Ag 3d_{3/2} and 3d_{5/2} is also characteristic of the metallic Ag 3d state [61].

3.3. Photodegradation of MO and photoreduction of Cr(VI)

The visible-light photocatalytic degradation of MO was selected as a model to investigate the photocatalytic activity of PMo₁₂/TiO₂/Ag composites. Fig. 4a presents the time profiles of photodegradation MO using PMo₁₂/TiO₂/Ag as catalysts under visible-light irradiation ($\lambda > 420$ nm). These as-prepared samples possess an adsorption capacity of MO molecules prior to light irradiation because of their mesoporous materials. Under the visible-light irradiation, pure TiO₂ exhibits negligible photocatalytic performance for the degradation of MO (5.4%) in 220 min due to its low visible-light response. For PMo₁₂/TiO₂, about 12.37% of MO (20 mL, 20 ppm) has been degraded, which is higher than that of TiO₂. Such results indicate that the introduction of PMo₁₂ into TiO₂ improved the photocatalytic activity under visible light irradiation.

When Ag NPs were deposited on the PMo₁₂/TiO₂ nanofibers, the photocatalytic activity of PMo₁₂/TiO₂/Ag was further enhanced. The MO (20 mL 20 ppm) can be completely degraded using PMo₁₂/TiO₂/Ag-3.98 as photocatalyst in 160 min, which is obviously higher than that of TiO₂/Ag (41.38%) and PMo₁₂/TiO₂ (7.50%). By increasing the content of Ag in the composites, it is found that PMo₁₂/TiO₂/Ag-5.41 represented the highest photocatalytic activity. The same amount of MO can be completely degraded in 120 min under visible-light irradiation (Fig. S9a). However, when more Ag NPs were loaded on the PMo₁₂/TiO₂ nanofibers, the resultant PMo₁₂/TiO₂/Ag-6.83 and PMo₁₂/TiO₂/Ag-7.19 composite catalysts require 200 and 220 min for the complete degradation of MO. Because the excessive Ag would occupy a portion of the active sites on the surface of PMo₁₂/TiO₂ fibers, thus it reduced the formation of active intermediate species and the surface adsorption capability of MO, resulting in the decrease of their photocatalytic performance [62,63]. In addition, there is a significant increase in the degradation rate of PMo₁₂/TiO₂/Ag during the photocatalytic process (from the degradation curves in Fig. 4a), which is

attributed to the photoreduction of the PMo₁₂. It is well known that polyoxoanion [PMo₁₂O₄₀]³⁻ has strong reversible redox property, which can be easily reduced. Under visible-light irradiation, [PMo₁₂O₄₀]³⁻ was photoreduced to heteropoly blue, which enhanced the visible-light absorption of PMo₁₂/TiO₂/Ag composites. The optical images and the UV–vis diffuse reflectance spectra of PMo₁₂/TiO₂/Ag-5.41 and PMo₁₂/TiO₂ before and after one cycle experiment present the color changes and the enhancement of visible-light absorption of the composites, respectively (Fig. S10–S13). With the enhancement of visible light absorption of PMo₁₂/TiO₂/Ag, its photogenerated carrier density is increased significantly, thus the photocatalytic activity of PMo₁₂/TiO₂/Ag composite has been improved, leading to the increase of MO degradation rate. In addition, the photocatalytic performance of PMo₁₂/TiO₂/Ag-5.41 under UV–vis light irradiation has also been greatly enhanced compared to PMo₁₂/TiO₂ (Fig. S14a), suggesting that the separation of photo-generated electrons and holes might be improved when Ag NPs were loaded.

In addition, the visible-light-driven photoreduction of Cr(VI) was also selected as the model to assess the photocatalytic activities of PMo₁₂/TiO₂/Ag for the removal of the inorganic pollutants. As shown in Fig. 4b, when no catalyst was added in the reaction, Cr(VI) just shows a slight photoreduction of 12.39%. When TiO₂ was applied as catalysts, the photoreduction efficiency of Cr(VI) is 13.07%. Such a little increase implied that TiO₂ may not possess the photocatalytic activity for the reduction of Cr(VI) under the visible light irradiation. However, when performed with PMo₁₂/TiO₂ and TiO₂/Ag catalyst, about 58.27% and 65.45% of Cr(VI) (40 mL 80 ppm) have been photoreduced in 60 min, meaning that the photoreduction efficiency of Cr(VI) have been enhanced by the introduction of PMo₁₂ and Ag NPs to TiO₂ substrates. For the PMo₁₂/TiO₂/Ag-X (X = 3.98, 5.41, 6.83, 7.19) composites, about 78.03, 79.10, 78.82 and 71.13% of Cr(VI) have been reduced in 60 min under visible-light irradiation ($\lambda > 420$ nm), respectively. PMo₁₂/TiO₂/Ag-5.41 still exhibits the highest activity for photoreduction of Cr(VI) (Fig. S9b).

As exhibited in Fig. 5a, the recycling tests reveal that the PMo₁₂/TiO₂/Ag-5.41 shows an ignorable loss of the photocatalytic activity for the degradation of MO after four cycles. It is worth mentioning that the degradation rate of MO in the second cycle was obviously increased owing to the strong reversible redox ability of PMo₁₂ polyoxoanion. PMo₁₂ could be photoreduced to heteropoly blue under visible light irradiation, which improved the visible-light absorption of PMo₁₂/TiO₂/Ag-5.41, leading to the increasing degradation efficiency of MO in the first cycle. This light activation was omitted, thus the enhanced degradation rate of MO was observed in the following recycles (Figs. S10–13). As shown in Fig. 5b, the photoreduction efficiency of Cr(VI)

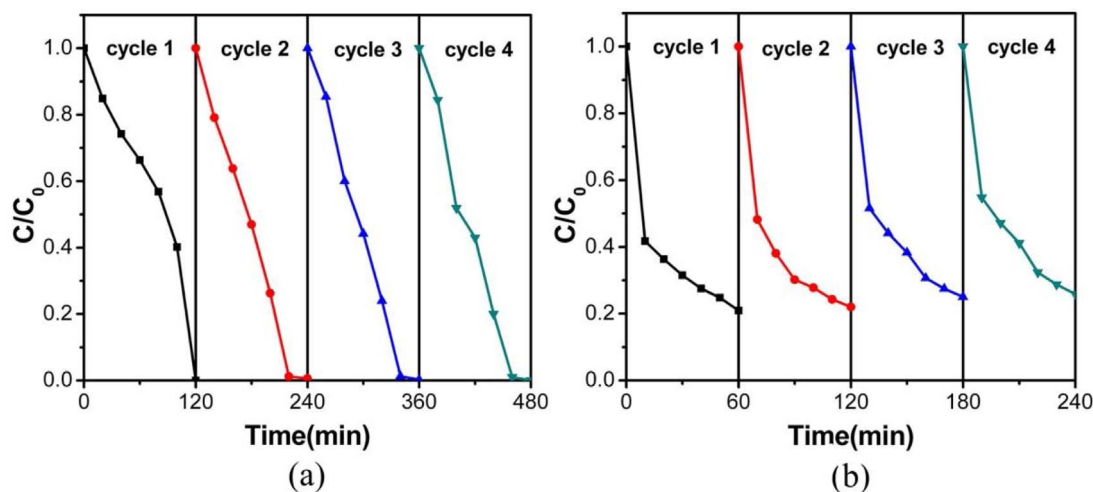


Fig. 5. Recycling experiments of (a) photocatalytic degradation of MO and (b) photoreduction of Cr(VI) employing PMo₁₂/TiO₂/Ag-5.41 as catalyst under visible-light irradiation ($\lambda > 420$ nm).

shows only a little decrease, which might be attributed to the loss of sample in the recycling process. The above results indicate that the PMo₁₂/TiO₂/Ag possesses excellent durability for the removal of organic and inorganic pollutants.

3.4. The photocatalytic mechanism

To verify the efficient separation of photoproduced charge carriers and the enhanced photocatalytic performance of as-obtained samples, the PL and EIS spectra were measured. The excitation wavelength of the PL spectra was 380 nm. It is well known that the recombination of electrons and holes can release energy in the form of PL emission. Hence, low PL intensity may suggest a low recombination rate of charge carriers, thus corresponding to a high photocatalytic activity. As illustrated in Fig. 6a, all samples show similar peaks centered at about 400 nm. The peak intensities of PL spectra for PMo₁₂/TiO₂ and TiO₂/Ag are decreased with respect to that of TiO₂, implying that the recombination of the photogenerated charge carrier has been inhibited by the introduction of PMo₁₂ and Ag NPs. After Ag was loaded on the PMo₁₂/TiO₂ fibers, PL intensity is dramatically decreased, revealing that the separation of photogenerated electrons and holes in PMo₁₂/TiO₂/Ag has been further enhanced. The PMo₁₂/TiO₂/Ag-5.41 has the lowest peak intensity, suggesting the best photogenerated charge carrier separation and the most efficient photocatalytic activity than the other samples. Fig. 6b exhibits the Nyquist plots of different electrodes. The radius of the arc on the EIS Nyquist plot can reflect the reaction rate occurring at the surface of electrode. Usually a small semicircle corresponds to a low charge transfer resistance (R_{ct}). It has been found that the R_{ct} values of PMo₁₂/TiO₂/Ag composites are much smaller than those of TiO₂, PMo₁₂/TiO₂ and TiO₂/Ag. PMo₁₂/TiO₂/Ag-5.41 possesses the smallest R_{ct} , indicating that the most effective separation of photoproduced electron-hole pairs and fast interfacial charge transfer rate would occur in the composite PMo₁₂/TiO₂/Ag-5.41 [64].

The transient photocurrent responses ($i-t$ curves) were also investigated to further confirm the charge carrier separation capacities of these photocatalysts. Fig. 6c exhibits the $i-t$ curves of pure TiO₂, PMo₁₂/TiO₂, TiO₂/Ag, PMo₁₂/TiO₂/Ag-5.41 under visible-light irradiation ($\lambda > 420$ nm), respectively. When the light was switched on and off during five circulations, the generated photocurrents are stable and reproducible. Upon visible-light irradiation, there is negligible photocurrent response for pure TiO₂. While the photocurrent density of PMo₁₂/TiO₂/Ag-5.41 (4.16×10^{-4} mA cm⁻²) is 2.05 and 1.45 times higher than that of PMo₁₂/TiO₂ (2.03×10^{-4} mA cm⁻²) and TiO₂/Ag (2.86×10^{-4} mA cm⁻²), respectively. These results demonstrate that

the separation efficiency of photogenerated electrons and holes, and the utilization of visible light in PMo₁₂/TiO₂/Ag-5.41 have been largely enhanced. Therefore, it can be inferred that the introduction of PMo₁₂ and Ag NPs to TiO₂ could accelerate the separation of photogenerated charge carriers and improve the photocatalytic activity of the composites.

In order to further prove the influence of Ag NPs on the photocatalytic activity of PMo₁₂/TiO₂/Ag, the $i-t$ curves with a band pass filter $\lambda = 550 \pm 20$ nm were measured (Fig. 6d). It can be clearly observed that PMo₁₂/TiO₂/Ag-5.41 has a much higher photocurrent density than that of PMo₁₂/TiO₂. This might be related to the SPR absorption of Ag NPs and the intense local electromagnetic fields caused by Ag NPs, which enhanced the visible-light response and promoted the charge separation of the composite. This result can be further demonstrated by the photodegradation of MO under $\lambda = 550 \pm 20$ nm light irradiation. As exhibited in Fig. S15, the MO degradation efficiency of PMo₁₂/TiO₂/Ag-5.41 is 17.23% in 5 h, which is much higher than PMo₁₂/TiO₂ (4.7%).

To further study the mechanism of MO photodegradation, we employed the hole and free radical trapping experiments. In this study, isopropanol (IPA, OH quencher) [65], 4-hydroxy-TEMPO (O_2^- quencher) [66] and triethanolamine (TEOA, h^+ quencher) [67] are adopted to find which reactive species are responsible for MO degradation. Firstly, the radical trapping test of PMo₁₂/TiO₂ (20% 450 °C) was studied (Fig. 7a). The addition of IPA decreases the degradation rate of MO, while TEMPO or TEOA has no effect on degradation efficiency. This experiment implies that the OH radical species play a significant role in the degradation process of MO for PMo₁₂/TiO₂, and the corresponding mechanism is provided as Fig. S16. For PMo₁₂/TiO₂/Ag-5.41, the degradation efficiency of MO was slightly reduced upon addition of TEOA (Fig. 7b), revealing that holes play little roles in the MO photodegradation process. However, the degradation rate of MO was significantly decreased when 0.5 mM of IPA or 0.2 mM of 4-hydroxy-TEMPO (or N_2 ; Fig. S17) was introduced into the reaction system. This result indicates that O_2^- and OH active species are the main reactive species in the process of MO degradation using PMo₁₂/TiO₂/Ag as catalysts under visible light irradiation.

On the basis of above results, the probable mechanisms for the degradation of MO and the photoreduction of Cr(VI) can be deduced as following. The LUMO and HOMO values of PMo₁₂ can be calculated via cyclic voltammetry and UV-vis diffuse reflectance spectra methods [68]. The band gap E_g of PMo₁₂ was estimated to be 2.4 eV from the K-M function (Fig. S18). As a result of cyclic voltammetry, the LUMO of PMo₁₂ is about 0.73 V (Fig. S19). Therefore the HOMO of PMo₁₂ is

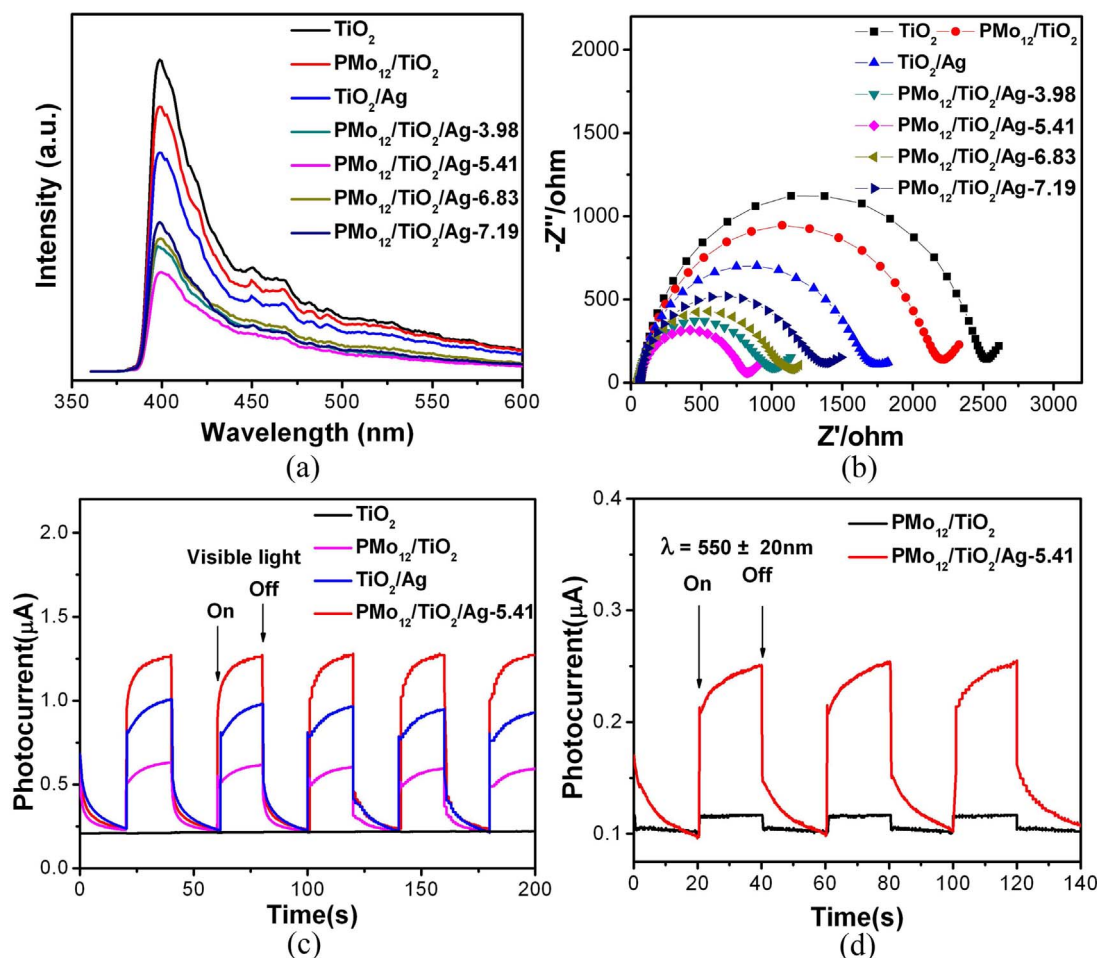


Fig. 6. The PL spectra (a) and the EIS Nyquist plots (b) of different samples; (c) The $i-t$ curves of pure TiO_2 , $\text{PMo}_{12}/\text{TiO}_2$, TiO_2/Ag , $\text{PMo}_{12}/\text{TiO}_2/\text{Ag-5.41}$ samples under visible-light irradiation ($\lambda > 420 \text{ nm}$); (d) The $i-t$ curves of $\text{PMo}_{12}/\text{TiO}_2$ and $\text{PMo}_{12}/\text{TiO}_2/\text{Ag-5.41}$ with a band pass filter $\lambda = 550 \pm 20 \text{ nm}$ in $0.5 \text{ M Na}_2\text{SO}_4$ aqueous solution at $+0.8 \text{ V vs. Hg/Hg}_2\text{Cl}_2$.

calculated to be 3.13 V ($E_{\text{HOMO}} = E_{\text{LUMO}} + E_g$). The results are consistent with the previous literature [68]. Hence, the degradation mechanism of MO can be illustrated as Fig. 7c. Both of PMo_{12} and Ag NPs can be excited under visible-light irradiation. The photoexcited holes of PMo_{12} can migrate to the VB of TiO_2 and react with H_2O to form OH. However, O_2^- could not be generated on the PMo_{12} surface owing to the LUMO of PMo_{12} (0.73 V vs NHE) is more positive than that of the O_2/O_2^- potential (-0.046 V vs NHE). At the same time, a great deal of electron-hole pairs was photogenerated due to the SPR absorbance of Ag NPs [69]. Because the LUMO potential of PMo_{12} (0.73 V vs NHE) is more negative than that of Ag^+/Ag ($+0.799 \text{ V vs NHE}$), therefore we deduce that the photogenerated electrons of PMo_{12} move to metallic Ag and combine with the plasmonic holes of Ag NPs [70–72]. Meanwhile, the hot plasmonic electrons of Ag could be trapped directly by the absorbed O_2 to form O_2^- . As a result, MO was efficiently degraded by the O_2^- and OH active species. The mechanism of photoreduction Cr(VI) is similar to that of photodegradation of MO (Fig. 7d). The hot plasmonic electrons from Ag NPs could reduce $\text{Cr}_2\text{O}_7^{2-}$ to Cr^{3+} species, while the photoexcited holes of PMo_{12} migrate to TiO_2 to participate in the oxidation reaction with $i\text{-PrOH}$. Consequently, the Cr(VI) was efficiently photoreduced by $\text{PMo}_{12}/\text{TiO}_2/\text{Ag}$ under visible-light irradiation.

4. Conclusions

In summary, we have prepared a new type of $\text{PMo}_{12}/\text{TiO}_2/\text{Ag}$ composite photocatalysts by using a facile and simple technique. These

composites exhibit highly efficient and recyclable photocatalytic performance for the removal of MO and Cr(VI) under visible-light irradiation ($\lambda > 420 \text{ nm}$). The excellent photocatalytic performances are ascribed to the enhanced visible-light absorption, and the effective separation of photogenerated charge carriers by depositing of PMo_{12} and Ag NPs on TiO_2 . Moreover, the reasonable mechanisms of the as-prepared composites working under the visible-light irradiation have been proposed based on the results of PL spectra, $i-t$ curves, and radical trapping tests, which provides some new ideas for the design and preparation of novel POMs-based plasmon photocatalysts with highly efficient photocatalytic performance under visible light irradiation.

Acknowledgements

We acknowledge the financial support from the National Natural Science Foundation of China (grant no. 21771033, 21671036, and 21401131), the Fundamental Research Funds for the Central Universities (grant no. 2412016KJ018) and Opening Project of Key Laboratory of Polyoxometalate Science of the Ministry of Education (grant no. 130014556).

Appendix A. Supplementary data

Supplementary data associated with this article can be found, in the online version, at <http://dx.doi.org/10.1016/j.apcatb.2017.09.027>.

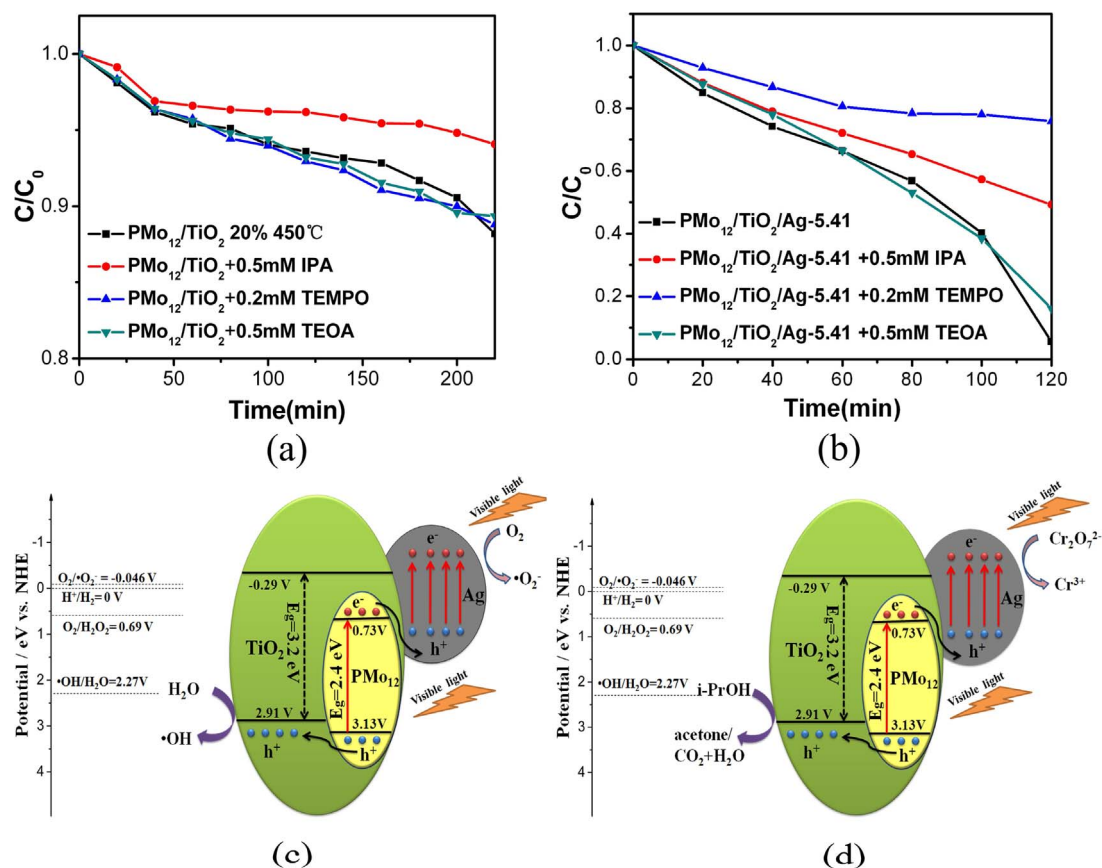


Fig. 7. The effects of various scavengers on the visible-light photodegradation of MO for (a) $\text{PMo}_{12}/\text{TiO}_2$ and (b) $\text{PMo}_{12}/\text{TiO}_2/\text{Ag-5.41}$, respectively; The photocatalytic reaction mechanism of (c) photodegradation of MO and (d) photoreduction of Cr(VI) for $\text{PMo}_{12}/\text{TiO}_2/\text{Ag}$ under visible-light irradiation ($\lambda > 420$ nm).

References

- [1] P. Miretzky, A.F. Cirelli, J. Hazard. Mater. 180 (2010) 1–19.
- [2] R.F. Dong, B.Z. Tian, C.Y. Zeng, T.Y. Li, T.T. Wang, J.L. Zhang, J. Phys. Chem. C 117 (2013) 213–220.
- [3] D.Z. Lu, P.F. Fang, X.Z. Liu, S.B. Zhai, C.H. Li, X.N. Zhao, J.Q. Ding, R.Y. Xiong, Appl. Catal. B 179 (2015) 558–573.
- [4] K.X. Li, L.S. Yan, Z.X. Zeng, S.L. Luo, X.B. Luo, X.M. Liu, H.Q. Guo, Y.H. Guo, Appl. Catal. B 156 (2014) 141–152.
- [5] Y. Yang, G.Z. Wang, Q. Deng, D.H.L. Ng, H.J. Zhao, ACS Appl. Mater. Interfaces 6 (2014) 3008–3015.
- [6] G. Yan, H.F. Shi, H.Q. Tan, W.B. Zhu, Y.H. Wang, H.Y. Zang, Y.G. Li, Dalton Trans. 45 (2016) 13944–13950.
- [7] M.R. Hoffmann, S.T. Martin, W.Y. Choi, D.W. Bahnemann, Chem. Rev. 95 (1995) 69–96.
- [8] A.L. Linsebigler, G.Q. Lu, J.T.Y. Jr., Chem. Rev. 95 (1995) 735–758.
- [9] T.R. Gordon, M. Cargnello, T. Paik, F. Mangolini, R.T. Weber, P. Fornasiero, C.B. Murray, J. Am. Chem. Soc. 134 (2012) 6751–6761.
- [10] J. Lee, M.C. Orillall, S.C. Warren, M. Kamperman, F.J. Disalvo, U. Wiesner, Nat. Mater. 7 (2008) 222–228.
- [11] H.G. Yang, C.H. Sun, S.Z. Qiao, J. Zou, G. Liu, S.C. Smith, H.M. Cheng, G.Q. Lu, Nature 453 (2008) 638–641.
- [12] R. Asahi, T. Morikawa, T. Ohwaki, K. Aoki, Y. Taga, Science 293 (2001) 269–271.
- [13] F. Zuo, K. Bozhilov, R.J. Dillon, L. Wang, P. Smith, X. Zhao, C. Bardeen, P.Y. Feng, Angew. Chem. Int. Ed. 51 (2012) 6223–6226.
- [14] E. Borgarello, J. Kiwi, M. Grätzel, E. Pelizzetti, M. Visca, J. Am. Chem. Soc. 104 (1982) 2996–3002.
- [15] W. Choi, A. Termin, M.R. Hoffmann, J. Phys. Chem. 98 (1994) 13669–13679.
- [16] D.R. Baker, P.V. Kamat, Adv. Funct. Mater. 19 (2009) 805–811.
- [17] C.B. Liu, L.L. Wang, Y.H. Tang, S.L. Luo, Y.T. Liu, S.Q. Zhang, Y.X. Zeng, Y.Z. Xu, Appl. Catal. B 164 (2015) 1–9.
- [18] C. Karakaya, Y. Türker, Ö. Dag, Adv. Funct. Mater. 23 (2013) 4002–4010.
- [19] H.F. Shi, H.Q. Tan, W.B. Zhu, Z.C. Sun, Y.J. Ma, E.B. Wang, J. Mater. Chem. A 3 (2015) 6586–6591.
- [20] L.L. Wang, X.D. Duan, G.M. Wang, C.B. Liu, S.L. Luo, S.Q. Zhang, Y.X. Zeng, Y.Z. Xu, Y.T. Liu, X.F. Duan, Appl. Catal. B 186 (2016) 88–96.
- [21] H.G. Yu, P. Xiao, J. Tian, F.Z. Wang, J.G. Yu, ACS Appl. Mater. Interfaces 8 (2016) 29470–29477.
- [22] R. Liu, P. Wang, X.F. Wang, H.G. Yu, J.G. Yu, J. Phys. Chem. C 116 (2012) 17721–17728.
- [23] Y.-Y. Bai, Y. Lu, J.-K. Liu, J. Hazard. Mater. 307 (2016) 26–35.
- [24] X. Xin, J.Y. Lang, T.T. Wang, Y.G. Su, Y.X. Zhao, X.J. Wang, Appl. Catal. B 181 (2016) 197–209.
- [25] S.S. Patil, M.G. Mali, M.S. Tamboli, D.R. Patil, M.V. Kulkarni, H. Yoon, H. Kim, S.S. Al-Deyab, S.S. Yoon, S.S. Kolekar, B.B. Kale, Catal. Today 260 (2016) 126–134.
- [26] S. Linic, P. Christopher, D.B. Ingram, Nat. Mater. 10 (2011) 911–921.
- [27] Z.Y. Zhang, Y.Z. Huang, K.C. Liu, L.J. Guo, Q. Yuan, B. Dong, Adv. Mater. 27 (2015) 5906–5914.
- [28] X.T. Wang, C.H. Liow, A. Bisht, X.F. Liu, T.C. Sum, X.D. Chen, S.Z. Li, Adv. Mater. 27 (2015) 2207–2214.
- [29] A.V. Rupa, D. Manikandan, D. Divakar, T. Sivakumar, J. Hazard. Mater. 147 (2007) 906–913.
- [30] K.H. Leong, B.L. Gan, S. Ibrahim, P. Saravanan, Appl. Surf. Sci. 319 (2014) 128–135.
- [31] R.A. Rather, S. Singh, B. Pal, Sol. Energy Mater. Sol. Cells 160 (2017) 463–469.
- [32] Y. Zhang, T. Wang, M. Zhou, Y. Wang, Z.M. Zhang, Ceram. Int. 43 (2017) 3118–3126.
- [33] X.F. Wang, T.Y. Li, R. Yu, H.G. Yu, J.G. Yu, J. Mater. Chem. A 4 (2016) 8682–8689.
- [34] H.Y. Guan, X.H. Wang, Y.H. Guo, C.L. Shao, X.T. Zhang, Y.C. Liu, R.-F. Louh, Appl. Surf. Sci. 280 (2013) 720–725.
- [35] L. Wang, C.B. Zhang, F. Gao, G. Mailhot, G. Pan, Chem. Eng. J. 314 (2017) 622–630.
- [36] Z.H. Kang, E.B. Wang, B.D. Mao, Z.M. Su, L. Gao, S.Y. Lian, L. Xu, J. Am. Chem. Soc. 127 (2005) 6534–6535.
- [37] D.L. Long, R. Tsunashima, L. Cronin, Angew. Chem. Int. Ed. 49 (2010) 1736–1758.
- [38] M. Sadakane, E. Steckhan, Chem. Rev. 98 (1998) 219–237.
- [39] A. Dolbecq, E. Dumas, C.R. Mayer, P. Mialane, Chem. Rev. 110 (2010) 6009–6048.
- [40] D.-Y. Du, J.-S. Qin, S.-L. Li, Z.-M. Su, Y.-Q. Lan, Chem. Soc. Rev. 43 (2014) 4615–4632.
- [41] J. Yin, L. Qi, H.Y. Wang, ACS Appl. Mater. Interfaces 3 (2011) 4315–4322.
- [42] N. Fu, G.X. Lu, Chem. Commun. 24 (2009) 3591–3593.
- [43] I.A. Weinstock, Chem. Rev. 98 (1998) 113–170.
- [44] A. Hiskia, A. Mylonas, E. Papaconstantinou, Chem. Soc. Rev. 30 (2001) 62–69.
- [45] H.-F. Shi, G. Yan, Y. Zhang, H.-Q. Tan, W.-Z. Zhou, Y.-Y. Ma, Y.-G. Li, W.-L. Chen, E.-B. Wang, ACS Appl. Mater. Interfaces 9 (2017) 422–430.
- [46] H.X. Jin, Q.Y. Wu, W.Q. Pang, J. Hazard. Mater. 141 (2007) 123–127.
- [47] R.R. Ozer, J.L. Ferry, Environ. Sci. Technol. 35 (2001) 3242–3246.
- [48] A. Pearson, S.K. Bhargava, V. Bansal, Langmuir 27 (2011) 9245–9252.
- [49] D.Y. Zhang, X. Li, H.Q. Tan, G.Q. Zhang, Z. Zhao, H.F. Shi, L.T. Zhang, W.X. Yu, Z.C. Sun, RSC Adv. 4 (2014) 44322–44326.
- [50] M. Yoon, J.A. Chang, Y. Kim, J.R. Choi, K. Kim, S.J. Lee, J. Phys. Chem. B 105

- (2001) 2539–2545.
- [51] J.A. Rengifo-Herrera, M.N. Blanco, L.R. Pizzio, *Appl. Catal. B* 110 (2011) 126–132.
- [52] J.A. Rengifo-Herrera, L.R. Pizzio, M.N. Blanco, C. Roussel, C. Pulgarin, *Photochem. Photobiol. Sci.* 10 (2011) 29–34.
- [53] L. Xu, X. Yang, Y.H. Guo, F.Y. Ma, Y.N. Guo, X. Yuan, M.X. Huo, *J. Hazard. Mater.* 178 (2010) 1070–1077.
- [54] H.X. Jin, Q.Y. Wu, W.Q. Pang, *J. Hazard. Mater.* 141 (2007) 123–127.
- [55] L. Li, Q.-Y. Wu, Y.-H. Guo, C.-W. Hu, *Microporous Mesoporous Mater.* 87 (2005) 1–9.
- [56] A.B. Murphy, *Sol. Energy Mater. Sol. Cells* 91 (2007) 1326–1337.
- [57] C. Cui, Y.P. Wang, D.Y. Liang, W. Cui, H.H. Hu, B.Q. Lu, S. Xu, X.Y. Li, C. Wang, Y. Yang, *Appl. Catal. B* 158 (2014) 150–160.
- [58] D.J. Wang, G.Q. Xue, Y.Z. Zhen, F. Fu, D.S. Li, *J. Mater. Chem.* 22 (2012) 4751–4758.
- [59] R.W. Liang, R. Chen, F.F. Jing, N. Qin, L. Wu, *Dalton Trans.* 44 (2015) 18227–18236.
- [60] J.K. Zhou, L. Lv, J.Q. Yu, H.L. Li, P.Z. Guo, H. Sun, X.S. Zhao, *J. Phys. Chem. C* 112 (2008) 5316–5321.
- [61] Z.Y. Chen, L. Fang, W. Dong, F.G. Zheng, M.R. Shen, J.L. Wang, *J. Mater. Chem. A* 2 (2014) 824–832.
- [62] G. Gyawali, R. Adhikari, B. Joshi, T.H. Kim, V. Rodríguez-González, S.W. Lee, *J. Hazard. Mater.* 263 (2013) 45–51.
- [63] Q. Xiang, G.F. Meng, H.B. Zhao, Y. Zhang, H. Li, W.J. Ma, J.Q. Xu, *J. Phys. Chem. C* 114 (2010) 2049–2055.
- [64] W.H. Leng, Z. Zhang, J.Q. Zhang, C.N. Cao, *J. Phys. Chem. B* 109 (2005) 15008–15023.
- [65] Y. Feng, J.C. Shen, Q.F. Cai, H. Yang, Q.H. Shen, *New J. Chem.* 39 (2015) 1132–1138.
- [66] Y.M. Chen, A.H. Lu, Y. Li, L.S. Zhang, H.Y. Yip, H.J. Zhao, T.C. An, P.-K. Wong, *Environ. Sci. Technol.* 45 (2011) 5689–5695.
- [67] J. Luo, X.S. Zhou, L. Ma, X.Y. Xu, *RSC Adv.* 5 (2015) 68728–68735.
- [68] J.-S. Li, X.-J. Sang, W.-L. Chen, L.-C. Zhang, Z.-M. Zhu, T.-Y. Ma, Z.-M. Su, E.-B. Wang, *ACS Appl. Mater. Interfaces* 7 (2015) 13714–13721.
- [69] K.H. Leong, B.L. Gan, S. Ibrahim, P. Saravanan, *Appl. Surf. Sci.* 319 (2014) 128–135.
- [70] Y.X. Tang, Z.L. Jiang, J.Y. Deng, D.G. Gong, Y.K. Lai, H.T. Tay, I.T.K. Joo, T.H. Lau, Z.L. Dong, Z. Chen, *ACS Appl. Mater. Interfaces* 4 (2012) 438–446.
- [71] X. Yan, X.Y. Wang, W. Gu, M.M. Wu, Y. Yan, B. Hu, G.B. Che, D.L. Han, J.H. Yang, W.Q. Fan, W.D. Shi, *Appl. Catal. B* 164 (2015) 297–304.
- [72] B.F. Luo, D.B. Xu, D. Li, G.L. Wu, M.M. Wu, W.D. Shi, M. Chen, *ACS Appl. Mater. Interfaces* 7 (2015) 17061–17069.